

A facile route to preparation of Co_3O_4 nanoplates and investigation of their charge storage ability as electrode material for supercapacitors

Mustafa Aghazadeh¹ · Rohollah Ahmadi² · Davoud Gharailou³ ·
Mohammad Reza Ganjali^{3,4} · Parviz Norouzi³

Received: 15 March 2016 / Accepted: 21 April 2016 / Published online: 27 April 2016
© Springer Science+Business Media New York 2016

Abstract A fast, cheap and facile method was developed for the preparation of Co_3O_4 nanoplates at large-scale. According to this method, initially $\beta\text{-Co}(\text{OH})_2$ nanoplates were prepared through a simple, template- and additive-free electrodeposition route and then the Co_3O_4 nanoplates were obtained via the calcination of the hydroxide precursor at 500 °C for 3 h, under an O_2 atmosphere. The products were characterized by XRD, IR, DCS-TG and SEM techniques, and electrochemical investigations by cyclic voltammetry, charge–discharge tests and EIS measurements, which confirmed the excellent supercapacitive performance of the Co_3O_4 nanoplates including their high contribution and electrochemical utilization in the redox reactions, reversible redox reactions, low diffusion resistance, high specific capacitance of 485 F g^{-1} , and an 84.1 % capacity retention after 3000 cycling at the applied discharge current density of 5 A g^{-1} .

1 Introduction

Cobaltic oxide (Co_3O_4) is a transition metal oxide with attractive electronic, optical, electrochemical, and electrocatalytic properties. Nanostructured Co_3O_4 has received considerable attention due to its potentials for application in supercapacitors [1–7], heterogeneous catalysts [8, 9], sensors [10–14] and Li-ion rechargeable batteries [15–17]. Among the various metal oxide candidates for supercapacitors (Mn_3O_4 , MnO_2 , V_2O_5 , NiO, etc.), Co_3O_4 has been reported as the most attractive material because of its good redox activity and high theoretical specific capacitance (3560 F g^{-1}) [18]. An electrode material to be used in a supercapacitor should have a sufficiently large electroactive surface area for good electrochemical performance as well as a fast faradic redox reaction. Large surface areas are also necessary to facilitate the electrolyte penetration at the electrode–electrolyte interface and to the bulk of electrode, which results in fast ion and electron transport kinetics of the resulting electrodes. It is well-known that the surface area of nanostructured materials is directly proportional to their size and morphology of the material. Thus, many efforts have been devoted to the preparation of a wide variety of nanostructured Co_3O_4 morphologies such as hollow structures [2, 3], nanosheets [4, 15, 19, 20], nanoflowers [21], needles [5], nanoplates [7, 22, 23], nanowires [24], nanopillars [25] and nanoflakes [26]. Research has revealed that sheet- or plate-like structures can very well improve the supercapacitive behavior of Co_3O_4 as the electrode material [19–22]. These nanostructures possess large material–electrolyte interface areas, increased electrolyte penetration into the electroactive materials, large inter-sheet spacings for the rapid ions transport, large surface areas for better electrochemical reactions, and high utilization of the electrode materials.

✉ Mustafa Aghazadeh
maghazadeh@aeoi.org.ir

¹ Nuclear Science and Technology Research Institute (NSTRI),
P.O. Box 14395-834, Tehran, Iran

² Chemistry Department, Saveh Branch, Islamic Azad
University, Saveh, Iran

³ Center of Excellence in Electrochemistry, Faculty of
Chemistry, University of Tehran, Tehran, Iran

⁴ Biosensor Research Center, Endocrinology and Metabolism
Molecular-Cellular Sciences Institute, Tehran University of
Medical Sciences, Tehran, Iran

So far, preparation of nanostructured Co_3O_4 through various chemical solution-based methods such as solvothermal [1, 2, 11], hydrothermal [3–6, 12], thermal decomposition [24], chemical bath deposition [10, 26] and pyrolysis [27] techniques has been reported. Further to these methods, cathodic electrodeposition followed by heat-treatment, can be applied as a powerful technique for the preparation of nanostructured Co_3O_4 with particular characteristics [23, 28–34]. In such a two-step route, hydroxide precursor [i.e. $\text{Co}(\text{OH})_2$] is initially electrodeposited from a nitrate and/or chloride bath via base (OH^-) electrogeneration and the product is next subjected to heat-treatment under a proper atmosphere and temperature to yield cobalt oxide.

During the course of this work, a simple and scalable route was developed for the large-scale preparation of Co_3O_4 nanoplates in the absence of additives, surfactants or templates. The product as next assessed in terms of its supercapacitive performance by means of cyclic voltammetry (CV), charge–discharge cycling and electrochemical impedance spectroscopy (EIS).

2 Experimental procedure

2.1 Chemicals

$\text{Co}(\text{NO}_3)_2 \cdot 6\text{H}_2\text{O}$ (Merck), polytetrafluoroethylene (PTFE, Merck), acetylene black and KOH (Merck) were used as received. All solutions were prepared using purified water by a UHQ Elga System. A 0.005 M aqueous solution of $\text{Co}(\text{NO}_3)_2 \cdot 6\text{H}_2\text{O}$ was prepared and used for the electrodeposition experiments.

2.2 The synthesis procedure

Cobalt hydroxide was deposited on the steel (316L) substrates in a two electrode electrochemical cell, including a stainless-steel cathode (size 5 cm × 2 cm) centered between two parallel graphite anodes. Before the electrodeposition step, the steel substrate was electrochemically polished as described elsewhere [35]. The cobalt hydroxide films were deposited from a 0.005 M aqueous solution of $\text{Co}(\text{NO}_3)_2 \cdot 6\text{H}_2\text{O}$ in the absence of additives and the deposition experiments were performed in a direct current (DC) mode while applying a current density of 1 mA cm⁻² ($I = 1 \text{ mA cm}^{-2}$). The deposition time and bath temperature were 30 min and 25 °C, respectively. After the electrodeposition step, the resulting $\text{Co}(\text{OH})_2$ was repeatedly washed with deionized water, and dried at 60 °C for 2 h, before the powder was heat treated under air atmosphere under an incremental heating regime changing at a 10 °C min⁻¹ rate up to 500 °C for 3 h, leading to the formation of the final product (i.e. Co_3O_4).

2.3 Instruments

The XRD patterns of the produced hydroxide and oxide samples were acquired using powder X-ray diffraction (XRD, Phillips PW-1800) with a Cu K α radiation source. The morphologies of both samples were assessed through scanning electron microscopy (LEO 1455VP) under an accelerating voltage of 30 kV. The FT-IR spectra of the samples were recorded by a Bruker Vector 22 FT-IR spectrometer within the range of 400–4000 cm⁻¹. Further the thermal behavior of the hydroxide samples was evaluated by DSC-TG using a thermoanalyzer (STA-1500) in a dry-air atmosphere at a temperature range of 25–600 °C and a heating rate of 5 °C min⁻¹, while it was being converted to the oxide product. Cyclic voltammetric (CV) and galvanostatic charge–discharge experiments were conducted by an AUTOLAB[®], Eco Chemie, PGSTAT 30instrument. The EIS studies were carried out from 10 kHz to 0.1 Hz with DC bias.

2.4 Electrochemical measurements

A three-electrode electrochemical cell, comprising Ag/AgCl (1 M KCl, saturated) and platinum wire as the reference and the counter electrodes, respectively, was used for the electrochemical measurements. A 1 M aqueous solution of KOH was used as the electrolyte.

The working electrode was prepared through mixing the prepared electroactive oxide powder, acetylene black, conducting graphite and polytetrafluoroethylene (PTFE) binder (at a 75:10:10:5 weight ratio). The mixture was next pressed under 10 MPa of pressure, into 1 cm² nickel foam and the resulting assembly was dried in an oven for 10 min at 60 °C (The mass of the electroactive material on the fabricated working electrode was 2.2 mg). The results of CV evaluations of the working electrodes, were recorded over a range of –0.2 to 0.6 V versus Ag/AgCl at the various scan rates (i.e. 2, 5, 10, 25, 50 and 100 mV s⁻¹).

The constant current charge–discharge tests were also conducted at current densities of 1, 2, 3, 5, 7, 10 and 20 A g⁻¹ within a potential range of –0.2 to 0.5 V and the EIS data were recorded in the frequency range of 0.1 Hz–10 kHz at the open circuit potential and an AC voltage of 5 mV.

3 Results and discussion

3.1 Deposition of $\beta\text{-Co}(\text{OH})_2$

Cobalt hydroxide was cathodically deposited from an 0.005 M $\text{Co}(\text{NO}_3)_2 \cdot 6\text{H}_2\text{O}$ solution in a two-step electrochemical and chemical route [35–38]. Potential

measurements during the deposition process (−1.21 V vs. Ag/AgCl) revealed that water reduction occurred in the electrochemical step under the applied conditions, which was indicated by the released H₂ gas bubbling on the cathode surface which was an indication of the electrolysis of water leading to the electrogeneration of hydroxide ions. Figure 1 illustrates a schematic presentation of the Co(OH)₂ formation stage at the cathode surface. The general step involving the formation of hydroxide ions; including the reduction of water and the electrogeneration of hydroxide and H₂, as well as the chemical reaction and formation of cobalt hydroxide are presented in Fig. 1a.

3.2 Heat-treatment and formation of Co₃O₄

At this stage, the deposit prepared during the former step, was heat-treated at 500 °C for 3 h, as schematically shown in Fig. 1b. The physico-chemical changes and the conversion stages during the heat treatment were monitored through DSC-TG analysis and the results are given Fig. 2.

Initially a gradual weight loss coming up to 1.7 %, was observed at 30–150 °C, which was attributed to the evaporation of water molecules adsorbed/trapped in the deposited nanoplates. Next a major weight loss profile was observed from 150 to 400 °C, due to the elimination of water and the formation of the oxide species, which accounted for a 13.4 % weight loss. This value was consistent with a 13.6 % value calculated for the conversion of Co(OH)₂ to Co₃O₄ [40]. Over 400 °C, only a small weight loss of about ~1.2 % was observed in the TG curve from 400 to 500 °C, which was attributed to the removal of

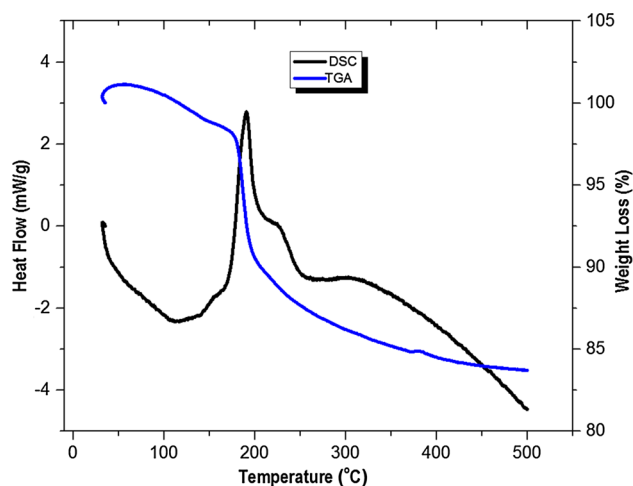


Fig. 2 Thermogravimetric analysis of the electrodeposited Co(OH)₂ sample

nitrate ions [41, 42]. The overall weight loss during the TG analysis of the transformation of cobalt hydroxide deposit to Co₃O₄ during by heating the sample up to 500 °C was 16.3 %. The following sequence, was hence proposed for the oxide formation during the heat-treatment [33, 34, 41]:

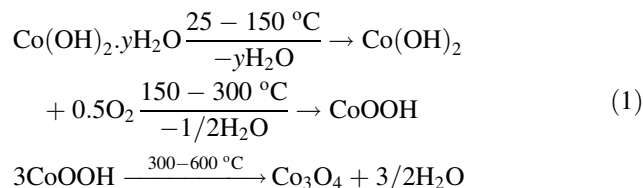
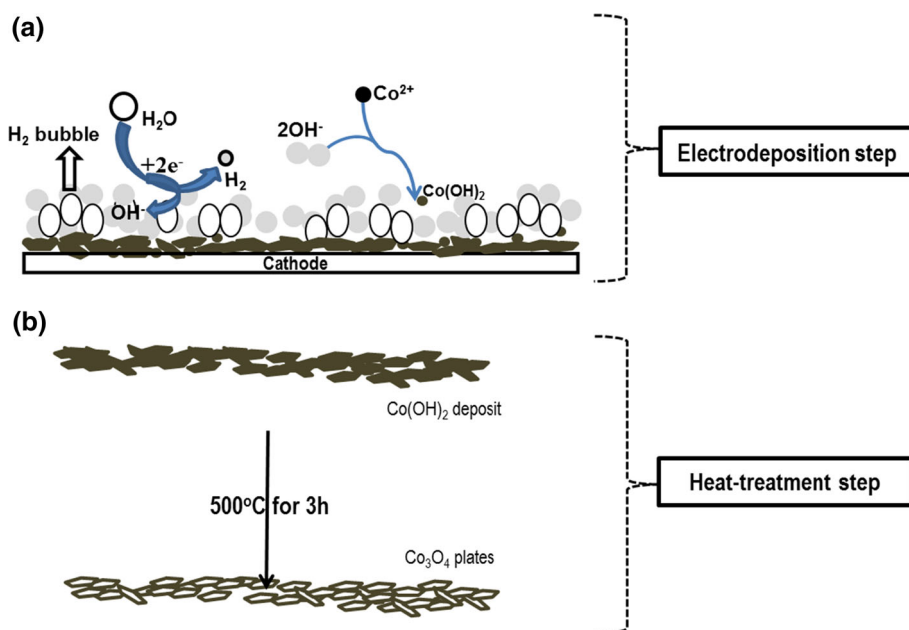


Fig. 1 Schematic view of Co₃O₄ preparation by electrodeposition-heat treatment step



3.3 Structural and morphological properties of the product

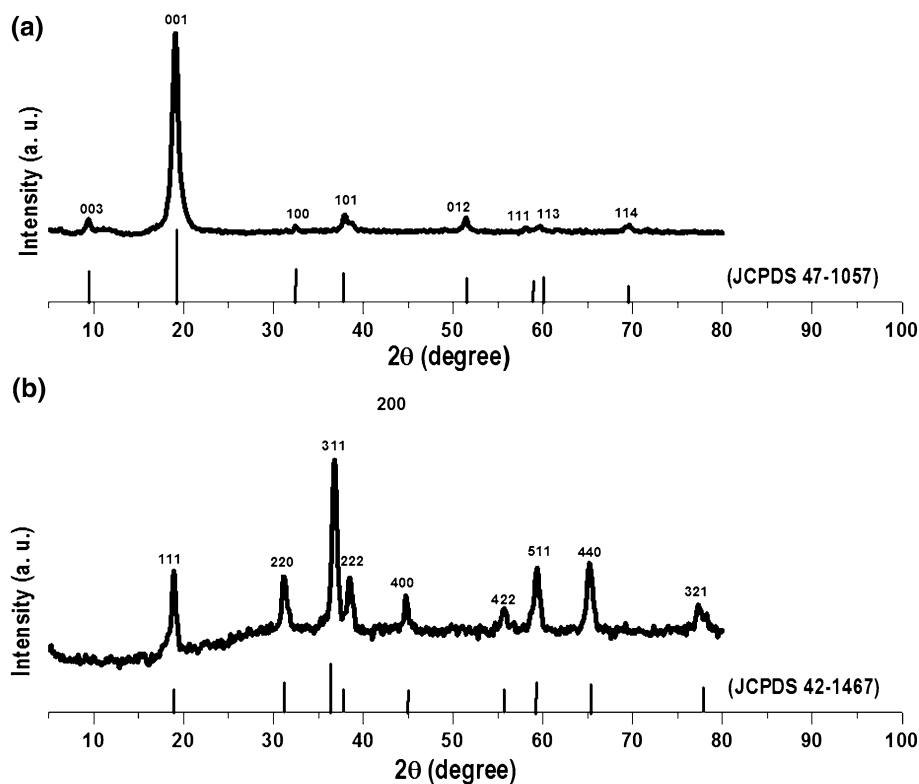
Figure 3 illustrates the XRD patterns of the prepared samples. The peaks in the XRD pattern of the hydroxide sample were found to fully match the hexagonal crystalline structure of β -Co(OH)₂ as donated by solid line in Fig. 3a (JCPDS File No. 30-443). No diffraction peaks corresponding to the α phase could be observed, indicating the high purity of the electrodeposited β -Co(OH)₂ prepared under the proposed electrochemical conditions. Figure 3b further shows the XRD pattern of the oxide sample resulting from the heat-treatment of electrodeposited β -Co(OH)₂, which contains all the nine typical diffraction peaks of the standard Co₃O₄ pattern (JCPDS 42-1467). The characteristic crystal planes of the prepared Co₃O₄ were (111), (220), (311), (222), (400), (422), (511), (440), and (531). No other phase peaks were observed, confirming the full conversion of the electrodeposited β -Co(OH)₂ into Co₃O₄ as a result of the heat-treatment at 500 °C, which was applied for 3 h.

The FTIR spectra of the β -Co(OH)₂ and Co₃O₄ nanoparticles are given in Fig. 4. The spectrum of the hydroxide sample contains (1) a narrow band located at 3628 cm⁻¹ corresponding to the stretching vibrations of the non-hydrogen bonded O–H in the brucite-like structure i.e. β -Co(OH)₂ [36–39]; (2) a broad band centered at 3451 cm⁻¹

corresponding to the stretching modes of the O–H in the interlayer water molecules and H-bound OH groups; (3) and a band located at 1632 cm⁻¹ also corresponding to the bending mode of water molecules; (4) two peaks at 1387 and 834 cm⁻¹ which could be attributed to the ν_3 and ν_2 vibrational modes of NO₃⁻ intercalated in the interlayers of Co(OH)₂, respectively [36]; (5) some peaks at 623, 526 and 480 cm⁻¹ indicating the Co–oxygen vibrations and Co–OH bending vibrations in the brucite-like octahedron [37]. The IR results were in support of a brucite-like structure for the product and also in agreement with the XRD observations.

Figure 2b represents the IR spectrum of the oxide sample obtained from heat-treatment of β -Co(OH)₂ sample. In the case of the oxide sample, two very strong peaks at 665 and 581 cm⁻¹, which are characteristic of spinel Co₃O₄ [43], appeared while those corresponding to β -Co(OH)₂ (i.e. 623 and 526 cm⁻¹) completely disappeared, indicating the full conversion of β -Co(OH)₂ to Co₃O₄. Remarkably, the bands at 565 and 652 cm⁻¹ were related to the OB3 (B represents Co³⁺ in an octahedral hole) and the ABO (A represents the Co²⁺ in a tetrahedral hole) vibrations in the spinel lattice, respectively [34, 41]. Furthermore, the peaks of the vibrational modes of NO₃⁻ (i.e. 1387 and 834 cm⁻¹) also disappeared in the spectra of the oxide sample. This further indicated the complete elimination of the intercalated nitrate ions during heat-treatment (as clearly seen in DSC-TG curves, Fig. 2). The two bands

Fig. 3 XRD patterns of the **a** electrodeposited and **b** heat treated samples



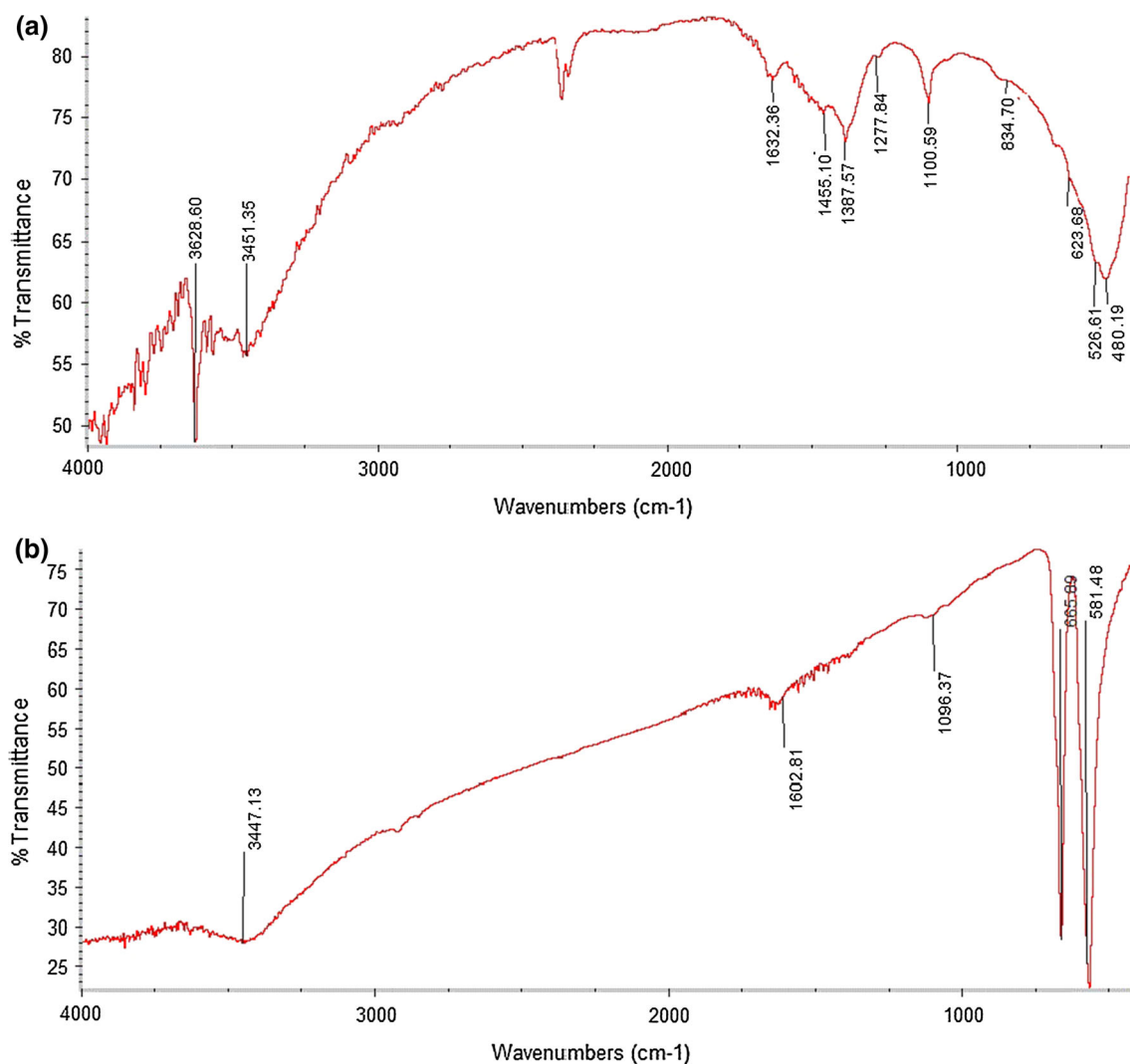


Fig. 4 IR spectra of **a** the electrodeposited sample and **b** heat-treated sample

at 3447 and 1602 cm^{-1} in Fig. 2b, could be associated to the hydroxyl groups of molecular H_2O . The peak at about 1096 cm^{-1} was also attributed to the vibrations of the carbonate groups originating from the reaction of oxide with air- CO_2 during the analysis procedure. These results were in complete accordance with those expected for the formation of Co_3O_4 .

Figure 5 illustrates the surface morphology of the prepared $\beta\text{-Co}(\text{OH})_2$ and Co_3O_4 samples. The SEM observations (in Fig. 5a) for the deposited sample indicated that the prepared cobalt hydroxide has composed of distinct plate-like structures in large quantity. High-magnification SEM image (Fig. 5b) clearly revealed that the observed plates are not perfect hexagons. In fact, the prepared $\beta\text{-Co}(\text{OH})_2$ plates have an irregularity or non-uniformity in the edge lengths. From Fig. 5b, the edge size of the $\beta\text{-Co}(\text{OH})_2$ plates was measured to be 200–300 nm. After heat-treatment, similar plate morphology was also

observed for the oxide sample (Fig. 5c, d). It was also observed that the Co_3O_4 plates have nano-uniform edge size with ranging from 200–300 nm.

3.4 Capacitance measurements

3.4.1 Cyclic voltammetry

To investigate the capacitive behavior of the electroactive Co_3O_4 ; CV, EIS and galvanostatic charge–discharge measurements were used. The CV curves were recorded at different scan rates of 2, 5, 10, 25, 50 and 100 mV s^{-1} in a 1 M KOH electrolyte. Figure 6a shows the CV profiles of the fabricated Co_3O_4 electrode at the scan rate of 10 mV s^{-1} . The CV curve in Fig. 7a, shows two clear pairs of redox peaks indicating the measured capacitance to be mainly based on redox reaction rather than EDLCs. Also, the relatively symmetric form of the oxidation and

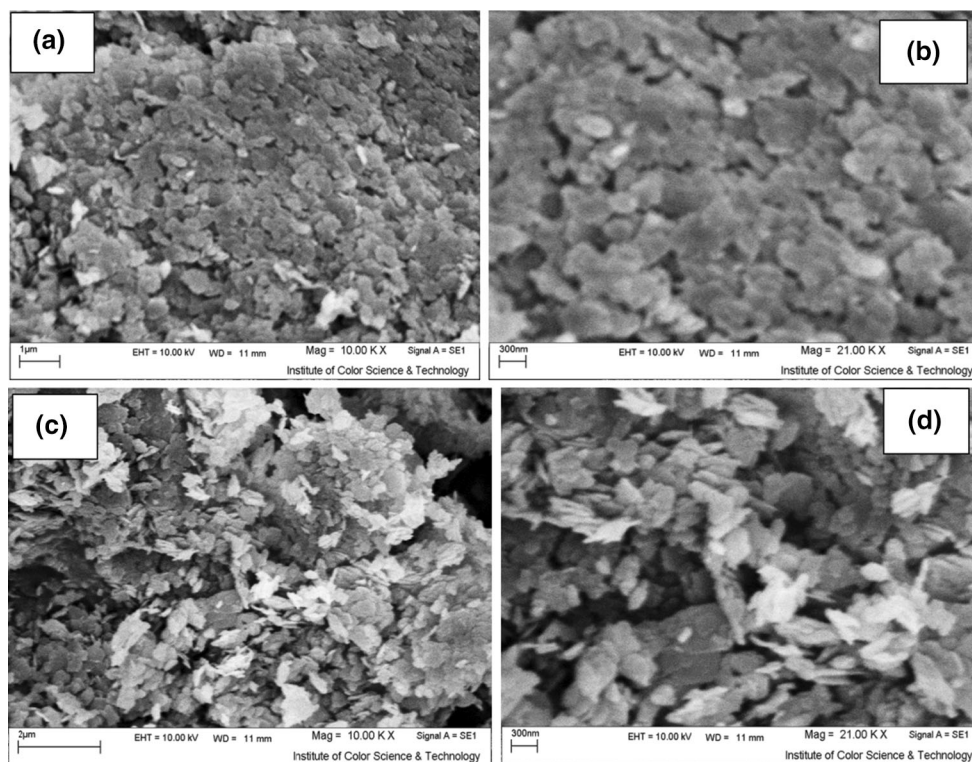
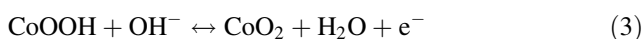


Fig. 5 SEM images of **a, b** electrodeposited $\text{Co}(\text{OH})_2$ and **c, d** final Co_3O_4 samples

reduction peaks indicate the fast and reversible redox process, as well the low Ohmic resistance and polarization as confirmed by EIS measurements (Fig. 8). These characteristics result from the large surface area and facilitate the penetration of electrolyte and/or the diffusion of OH^- in Co_3O_4 electrode. The observed peaks could be explained based on the reactions [5, 6]:



The peaks actually appear due to the $\text{Co}^{2+}/\text{Co}^{3+}$ reaction, as well as, the inter-conversion of Co^{3+} and Co^{4+} . From the CVs in Fig. 6b, the average specific capacitance of the Co_3O_4 electrode was estimated through integrating the area under the current–potential curve [7]:

$$C = \frac{1}{mv(V_a - V_c)} \int_{V_a}^{V_c} I(V) dV \quad (4)$$

where C is specific capacitance (SC) of Co_3O_4 (F g^{-1}) measured in the potential window of ΔV ($V_a - V_c$), m is the mass of Co_3O_4 (g), v is the scan rate (V s^{-1}) and I (V) is a current response depending on sweep voltage. From Eq. (4), it was concluded that the Co_3O_4 nanoplates possessed SCs of 605, 545, 490, 416, 356, 300 and 224 F g^{-1} at the respective scan rates of 1, 2, 5, 10, 25, 50 and

100 mV s^{-1} . The values indicated the excellent supercapacitive performance of the nanoplates.

The supercapacitive behavior versus scan rate (Fig. 7c) was further plotted, revealing that the SC decreases upon increasing the scan rate (SR). This suggested the observed capacitance to be mainly the result of the redox reaction. The CV profile was also found to be consistent with a redox mechanism for charge storage in Co_3O_4 , according to which under lower scan rate regimes, all of the electrode material mass is accessible for the ions, which is of course not possible at higher scan rates at which the ions might not find the opportunity to reach the inner sites of the nanostructured material. The decrease in the SC was not sharp however, which was held as proof that the OH^- ions can readily penetrate the electrode material. This way the electrode material may act as a buffer reservoir that can house the basic species reducing the ion transport path, and moderating the decrease in SC.

3.4.2 Charge–discharge tests

To obtain further information on the capacitance performance of the fabricated Co_3O_4 electrode, its galvanostatic discharge profiles were recorded at different current densities and its SC values were next calculated using the following equation:

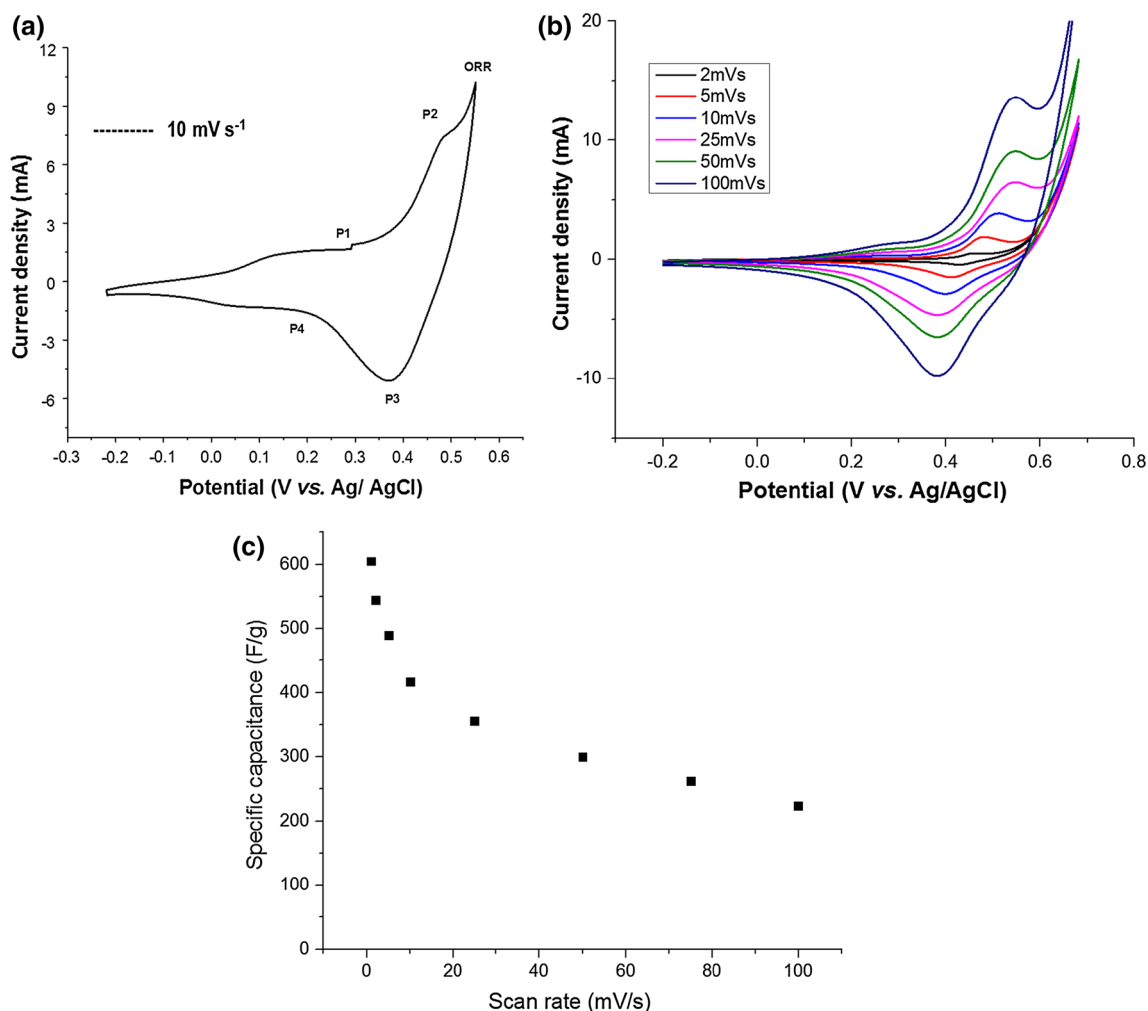


Fig. 6 **a** CV of Co₃O₄ electrode at the scan rate of 10 mV s⁻¹ and **b** at different scan rates and **c** its calculated specific capacitances

$$C = [I \times \Delta t] / (m \times \Delta V) \text{ (F/g)} \quad (5)$$

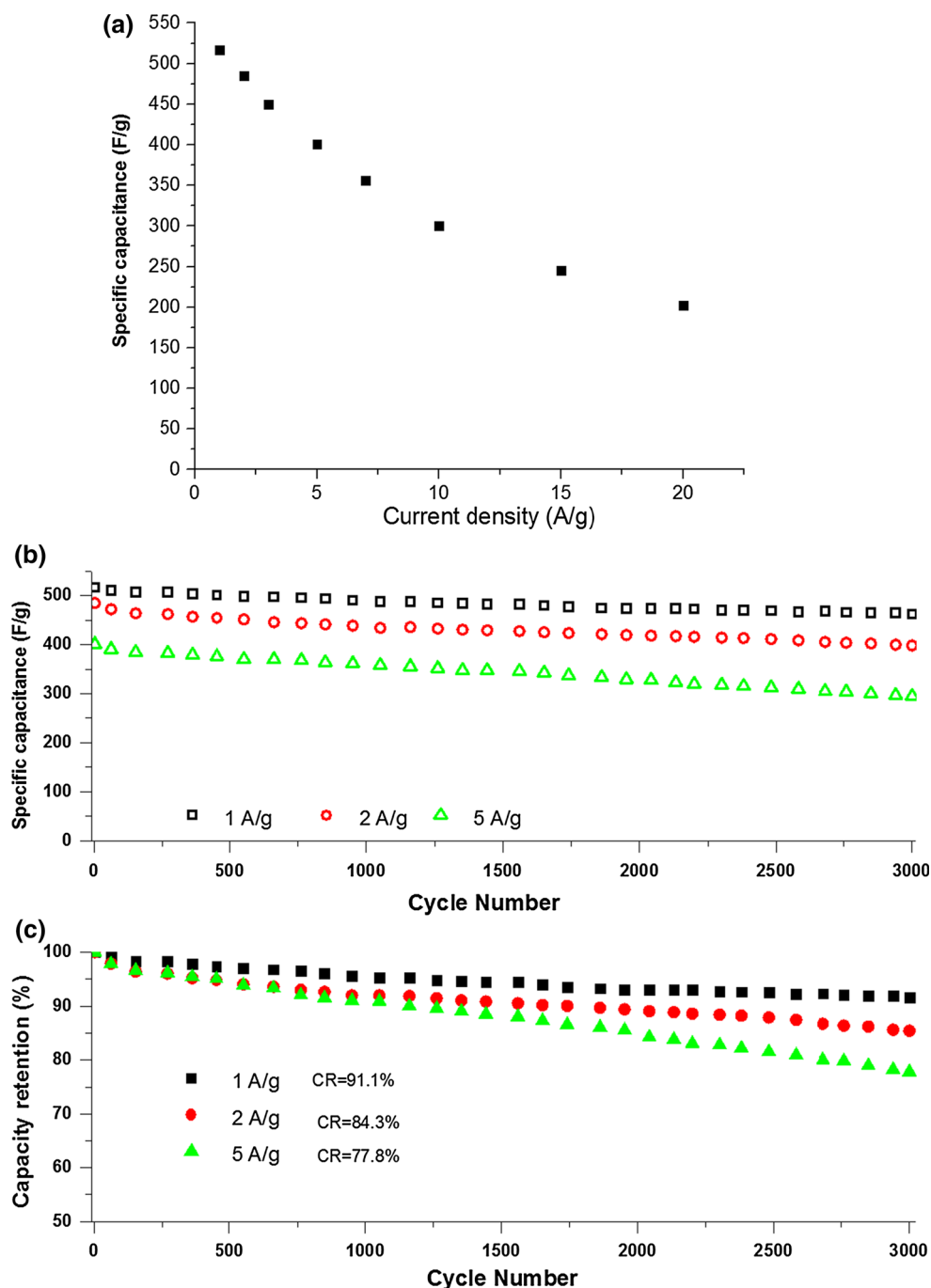
where C is the specific capacitance; I is the applied constant current (A), ΔV is the potential range (0.7 V), Δt is the time of a discharge cycle (s) and m is the mass of Co₃O₄ nanoplates (g).

Figure 7a illustrates the SC values of the electrode at different current loads. The results indicate that the nanoplates have been capable of delivering capacitance values as high as 517, 485, 450, 401, 300 and 202 F g⁻¹ at applied current densities of 1, 2, 3, 5, 10 and 20 A g⁻¹, respectively (Fig. 7a). These values were in agreements with those calculated from the CVs (Fig. 6c) and also confirmed the excellent supercapacitive behavior for the Co₃O₄ nanoplates.

Furthermore, the observed capacitance values were comparable with those for nanostructured Co₃O₄ prepared by different synthesis methods (e.g. 351 F g⁻¹ at 0.85 A g⁻¹ for Co₃O₄@Ni foam electrode prepared by participation-calcination [4], 405 and 641 F g⁻¹ at

1 A g⁻¹ for pure Co₃O₄ and Co₃O₄/graphene nanosheets prepared by chemical reaction followed by calcination [5], 574 F g⁻¹ at 0.1 A g⁻¹ for nanotubes prepared through chemical deposition followed by calcination [10], 454 F g⁻¹ at 2 A g⁻¹ for hierarchically porous film prepared by the hydrothermal method [12], 1033.3 F g⁻¹ at 2.5 A g⁻¹ for nanosheets prepared through an electrodeposition step followed by UV–ozone treatment [13], 443 F g⁻¹ at 2 A g⁻¹ for hierarchically porous films prepared by cathodic electrodeposition via liquid crystalline template [14], 393.6 F g⁻¹ at 1 A g⁻¹ for nanosheets prepared by cathodic electrodeposition followed by heat-treatment [15], 325 F g⁻¹ at 2 A g⁻¹ for porous nano-wall films prepared by cathodic electrodeposition [19], 519 F g⁻¹ at 1 mA cm⁻² for nanoparticles prepared by microwave assisted synthesis [20], and 1033.3 F g⁻¹ at 2.5 A g⁻¹ for nanosheets prepared by one-step potentiostatic method, followed by an UV–ozone treatment [23].

Fig. 7 **a** Calculated capacitances of Co_3O_4 electrode at the current densities and its long-term stabilities; **b** capacitance value and **c** capacity loss versus cycle number at the current densities



To evaluate the cyclability of the Co_3O_4 electrodes, the SCs and cycling stability (3000 cycles) were measured in a 1 M KOH electrolyte at the constant current density of 1, 2 and 5 A g^{-1} . Figure 7b, c represent the calculated SCs and the capacity retention values for the fabricated electrodes, when cycled up to 3000 cycles. Notably, the specific capacitance of each cycle was calculated via Eq. (5), and based on the obtained capacitance values the capacity retention of the Co_3O_4 electrode on cycling was evaluated. It was observed that the prepared nanoplates possessed high, stable capacitance values during cycling while they

exhibited excellent specific capacitance retention values of ca. 91.1, 84.3 and 77.8 % of its initial SC after 3000 continuous charge–discharge cycles. Thus, it was concluded that Co_3O_4 nanoplates can be suitable for long-time capacitor applications in KOH.

3.4.3 ESI measurement

The electrochemical behavior of the fabricated electrodes was further investigated by EIS measurements. Figure 8 contains the Nyquist plot of the fabricated Co_3O_4 electrode,

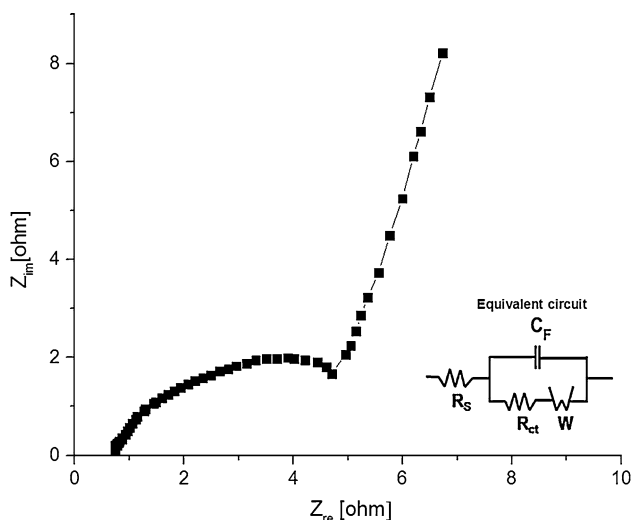


Fig. 8 EIS plot of the Co_3O_4 electrode in 1 M KOH solution. The inset shows the equivalent circuit

measured in the frequency range of 0.1 Hz–10 kHz at an open circuit potential, which is in the form of a semicircle over the high frequency range, followed by a straight sloped line in the low frequency region. The plot can be the result of an equivalent circuit comprising of an electrolyte resistance (R_s), double layer capacitance behavior (C_{dl}), charge transfer resistance (R_{ct}), Warburg element (Z_w) and pseudocapacitance (C_p) as shown in the inset of Fig. 8. The diameter of the semicircle corresponds to the interfacial charge-transfer resistance (i.e. R_{ct}), also referred to as the Faraday resistance. The calculated R_s and R_{ct} of the Co_3O_4 electrode were 0.73 and 4.3 Ω respectively. Such a low ESR and Faraday resistance provides the prepared electrode with the ability to exhibit an excellent supercapacitive performance. Furthermore, the nearly ideal straight line along the imaginary axis at the lower frequencies indicated that the Co_3O_4 nanoplates have a low diffusion resistance as can be inferred from the shape of CV curves. The EIS results confirmed the excellent electrochemical capacitive properties of the Co_3O_4 electrode.

4 Conclusion

Uniform and well-defined nanoplates of Co_3O_4 were obtained by a two-step of cathodic deposition followed by heat-treatment method. The DC electrodeposition from an additive free 0.005 M cobalt nitrate electrolyte resulted in the formation of $\beta\text{-Co}(\text{OH})_2$ nanoplates the heat treatment of which at 500 $^\circ\text{C}$ for 3 h, produced the oxide nanoplates. The electrochemical measurements revealed the Co_3O_4 nanoplates to display an excellent capacitive behavior with a specific capacitance of 517 F g^{-1} at a current density of 1 A g^{-1} and a good log-term cycle life of ca. 91 % after

3000 continuous charge–discharge cycles at the applied current density of 1 A g^{-1} . EIS analyses confirmed that, based on its low diffusion resistance and fast redox reaction, Co_3O_4 nanoplates can be excellent electro-active supercapacitor materials.

References

1. R. Pavul Raj, P. Ragupathy, S. Mohan, J. Mater. Chem. A **3**, 24338 (2015)
2. T. Meng, Q.Q. Xu, Z.H. Wang, Y.T. Li, Z.M. Gao, X.Y. Xing, T.Z. Ren, Electrochim. Acta **180**, 104 (2015)
3. X. Zhou, X. Shen, Z. Xia, Z. Zhang, J. Li, Y. Ma, Y. Qu, ACS Appl Mater. Interfaces **7**, 20322 (2015)
4. F. Manteghi, H. Kazemi, M. Peyvandipour, A. Asghari, RSC Adv. **5**, 76458 (2015)
5. A.N. Naveen, P. Manimaran, S. Selladurai, J. Mater. Sci. Mater. Electron. **26**, 8988 (2015)
6. H. Lin, Q. Huang, J. Wang, J. Jiang, F. Liu, Y. Chen, C. Wang, D. Lu, S. Han, Electrochim. Acta **191**, 444 (2016)
7. Z. Hai, L. Gao, Q. Zhang, H. Xu, D. Cui, Z. Zhang, D. Tsoukalas, J. Tang, S. Yan, Appl. Surf. Sci. **361**, 57 (2016)
8. S. Ali Khan, S. Bahadar Khan, A.M. Asiri, J. Mater. Sci. Mater. Electron. **27**, 5294 (2016)
9. F.L.S. Carvalho, Y.J.O. Asencios, J.D.A. Bellido, E.M. Assaf, Fuel Process. Technol. **142**, 182 (2016)
10. N.M. Shaalan, M. Rashad, A.H. Moharram, M.A. Abdel-Rahim, Mater. Sci. Semicond. Process. **46**, 1 (2016)
11. H. Che, A. Liu, J. Hou, J. Mu, Y. Bai, S. Zhao, X. Zhang, H. He, J. Mater. Sci. Mater. Electron. **25**, 3209 (2014)
12. Z. Gao, L. Zhang, C. Ma, Q. Zhou, Y. Tang, Z. Tu, W. Yang, L. Cui, Y. Li, Biosens. Bioelectron. **80**, 511 (2016)
13. B. Wu, L. Wang, H. Wu, K. Kan, G. Zhang, Y. Xie, Y. Tian, L. Li, K. Shi, Microporous Mesoporous Mater. **225**, 154 (2016)
14. L.T. Hoa, J.S. Chung, S.H. Hur, Sens. Actuators B Chem. **223**, 76 (2016)
15. Y. Zhu, Y. Chu, J. Liang, Y. Li, Z. Yuan, W. Li, Y. Zhang, X. Pan, S.L. Chou, L. Zhao, R. Zeng, Electrochim. Acta **190**, 843 (2016)
16. R. Gao, J. Zhu, X. Xiao, Z. Hu, J. Liu, X. Liu, J. Phys. Chem. C **119**, 4516 (2015)
17. J. Wu, L. Zuo, Y. Song, Y. Chen, R. Zhou, S. Chen, L. Wang, J. Alloys Compd. **656**, 745 (2016)
18. W. Liu, X. Li, M. Zhu, X. He, J. Power Sources **282**, 179 (2015)
19. X. Pan, X. Chen, Y. Li, Z. Yu, Electrochim. Acta **182**, 1101 (2015)
20. K. Qiu, Y. Lu, J. Cheng, H. Yan, X. Hou, D. Zhang, M. Lu, X. Liu, Y. Luo, Electrochim. Acta **157**, 62 (2015)
21. H. Che, A. Liu, J. Mater. Sci. Mater. Electron. **26**, 4097 (2015)
22. F. Wang, C. Lu, Y. Qin, C. Liang, M. Zhao, S. Yang, Z. Sun, X. Song, J. Power Sources **235**, 67 (2013)
23. C.W. Kung, H.W. Chen, C.Y. Lin, R. Vittal, K.C. Ho, J. Power Sources **214**, 91 (2012)
24. M. Ghiasi, A. Malekzadeh, H. Mardani, Mater. Sci. Semicond. Process. **42**, 311 (2016)
25. Y. Zheng, Z. Li, J. Xu, T. Wang, X. Liu, X. Duan, Y. Ma, Y. Zhou, C. Pei, Nano Energy **20**, 94 (2016)
26. Z. Han, X. Zheng, S. Yao, H. Xiao, F. Qu, X. Wu, Appl. Surf. Sci. **365**, 240 (2016)
27. R. Manogowri, R. Mary Mathelane, S. Valanarasu, I. Kulandaisamy, A. Benazir Fathima, A. Kathalingam, J. Mater. Sci. Mater. Electron. **27**, 3860 (2016)

28. G.P. Kim, I. Nam, N.D. Kim, J. Park, S. Park, J. Yi, *Electrochem. Commun.* **22**, 93 (2012)
29. A.D. Jagadale, V.S. Kumbhar, C.D. Lokhande, *J. Colloid Interface Sci.* **406**, 225 (2013)
30. A.D. Jagadale, V.S. Kumbhar, R.N. Bulakhe, C.D. Lokhande, *Energy* **64**, 234 (2014)
31. Y.F. Yuan, X.H. Xi, J.B. Wu, X.H. Huang, Y.B. Pei, J.L. Yang, S.Y. Guo, *Electrochem. Commun.* **13**, 1123–1126 (2011)
32. M. Aghazadeh, *J. Appl. Electrochem.* **42**, 89 (2012)
33. M. Aghazadeh, M. Hosseini-fard, B. Sabour, S. Dalvand, *Appl. Surf. Sci.* **287**, 187 (2013)
34. P. Razmjoo, B. Sabour, S. Dalvand, M. Aghazadeh, M.R. Ganjali, *J. Electrochem. Soc.* **161**, D293 (2014)
35. M. Aghazadeh, S. Dalvand, *J. Electrochem. Soc.* **161**, D18 (2014)
36. M. Aghazadeh, A.A.M. Barmi, T. Yousefi, *J. Iran. Chem. Soc.* **9**, 225 (2012)
37. M. Aghazadeh, S. Dalvand, M. Hosseini-fard, *Ceram. Int.* **40**, 3485 (2014)
38. M. Aghazadeh, H.M. Shiri, A.A.M. Barmi, *Appl. Surf. Sci.* **273**, 237 (2013)
39. M. Aghazadeh, A.A.M. Barmi, D. Gharailou, M.H. Peyrovi, B. Sabour, F. Najafi, *Appl. Surf. Sci.* **283**, 871 (2013)
40. J.P. Cheng, X. Chen, J.S. Wu, F. Liu, X.B. Zhang, V.P. Dravid, *CrystEngComm* **14**, 6702 (2012)
41. Z.P. Xu, H.C. Zeng, *Chem. Mater.* **11**, 67 (1999)
42. Z. Liu, R. Ma, M. Osada, K. Takada, T. Sasaki, *J. Am. Chem. Soc.* **127**, 13869 (2005)
43. Y.G. Li, B. Tan, Y.Y. Wu, *J. Am. Chem. Soc.* **128**, 14258 (2006)